Confinement Suppressed Phase Transition and Dynamic Self-Assembly of Ionic Superdiscs in Ordered Nanochannels: Implications for Nanoscale Applications

Mohamed Aejaz Kolmangadi[1], Li Zhuoqing[2], Glen J. Smales[1], Brian R. Pauw[1], Eugen Wuckert[3], Aileen Raab[3], Sabine Laschat[3], Patrick Huber[2,4,5], and Andreas Schönhals[1,*]

[1]Bundesantalt für Materialforschung und -prüfung (BAM), 12205 Berlin, Germany
[2]Hamburg University of Technology, Institute for Materials and X-Ray Physics, 21073 Hamburg, Germany
[3]Institut für Organische Chemie, Universität Stuttgart, 70569 Stuttgart, Germany

[4]Centre for X-Ray and Nano Science CXNS, Deutsches Elektronen-Synchrotron, Notkestr. 85 22607 Hamburg, Germany

[5]Center for Hybrid Nanostructures CHyN, University Hamburg, 22607 Hamburg, Germany

[*]CORRESPONDING AUTHOR: A. Schönhals, Bundesanstalt für Materialforschung und -prüfung (BAM), Unter den Eichen 87, 12205 Berlin, Germany; Tel. +49 30 / 8104-3384; Fax: +49 30 / 8104-73384; Email: Andreas.Schoenhals@bam.de

Abstract

Ionic Liquid Crystals are ionic liquids that exhibit liquid crystalline mesomorphism together with ionic conductivity. As known confined liquid crystal mesophases can show an anomalous dynamics and phase behavior. Investigations considering the factors controlling the macroscopic properties of ILCs in confinement are scare in the literature. This study reports the molecular mobility, and the phase transition behavior of a guanidinium based columnar ILC confined in the nanopores of self-ordered anodic aluminum oxide membranes of various pore diameters (25 – 180 nm) using Broadband Dielectric Spectroscopy (BDS), calorimetry and X-ray scattering. It is aimed to reveal in which way the pore size as well as the pore surface wettability (hydrophobic or hydrophilic) alters the molecular dynamics, and phase transition behavior for this system. These properties are crucial for applications. The DSC investigations reveal: (i) the phase transition temperature for the transition from the plastic crystalline to the crystalline-liquid state has non-monotonic dependence versus the inverse pore diameter and (ii) the transition from the liquid crystalline to the isotropic phase is suppressed for all nanoconfined samples. This transition suppressed in the thermal signal was evidenced by BDS and X-ray scattering. It is discussed as a continuous phase transition taking place in the pores instead of a discontinuous first order transition as observed for the bulk. BDS investigations show different relaxation processes for the bulk and the nanoconfined ILC. Molecular origins for various relaxation processes are discussed and suggested. It is further shown that the self-assembly of this ILC is dynamic in nature which might apply for other ILCs too. The obtained results will have implications for the nanoscale applications of ionic liquid crystals.

Keywords: Ionic liquid crystals, Nanoscale confinement, Broadband Dielectric Spectroscopy, Calorimetry, X-ray scattering

Introduction

Ionic Liquid Crystals (ILCs) are novel functional materials combining the characteristics of ionic liquids (ILs) and liquid crystals (LCs). The building molecules exhibit shape anisotropy, which leads to partial ordering into liquid crystals along with ionic conductivity like ionic liquids.[1,2] ILCs can be processed by several low-cost techniques and are potential materials for opto-electronic and for biological applications because ILCs are often water soluble and align on substrates[3]. Some applications of ILCs include host frameworks to separate species based on size discrimination, and shape[4], and as nanofiltration membranes for water purification[5], as well as disinfectants for virus rejection[6]. ILCs that self-assemble into one-dimensional columns arranged in a 2D hexagonal lattice are referred as columnar ILCs. The one-dimensional columns can act as transport medium for instance for water[7], and importantly for ions[8]. The macroscopically aligned columns can act as a nanoporous membrane for water purification and proton conduction[9]. Thus, columnar ILCs enable an ordered and directed charge transport leading to further applications including electrolytes for batteries[10], in solar cells[11], and as membranes in biology[12].

Investigations on guanidinium based columnar ILCs in the bulk state include, the influence of the cation headgroup as well as the length of the alkyl chain concerning the stability of the mesophase including charge transport[13],[14]. Slight variations in the molecular structure directly alter the macroscopic properties of the system. On the one hand ILCs with a cyclic cation headgroup have a higher DC conductivity and faster molecular dynamics compared to their acyclic counterpart[13]. On the other hand, a systematic variation of the length of the alkyl chain in ILCs revealed that ILCs with alkyl side chain length of 8 and 10, behave more like ionic liquids with a narrow mesophase window, while the long chain ILCs (alkyl side chain lengths 12,14,16) show a broad mesophase range but a reduced electrical conductivity[14].

The nano-confinement of ILs can lead to both an increase and decrease of the ionic conduction compared to the bulk. Recently, Tu and coworkers confined a pyrrolidinium based IL with cation side chain length of 6 and 10 in porous anodic aluminum oxide with pore sizes of 80 and 10 nm. They observed an enhanced electrical conductivity for the IL with short side chain length, while a 300-fold decrease in the ionic conductivity for the IL having the longer side chain is found[15,16]. The different conduction behavior of the nano-confined long and short chain ILs remains unexplained. For conventional LCs confined in porous anodic aluminum oxide, some common features were observed: (i) usually the dynamics slows down in comparison to

the bulk and (ii) a decrease of the transition temperatures occur, where their pore size dependence often follows the Gibbs-Thomson relation[17,18].

Only a handful of investigations report the effect of a nano-confinement on ILCs. For a smectic ILC confined in porous anodic aluminum oxide a suppression of the smectic–isotropic phase transition was observed[19]. However, for a smectic ILC confined to mesopores the smectic-isotropic phase transition was observed where the phase transition temperature decreases as a function of inverse pore size, obeying the Gibbs-Thomson relation[20]. This indicates that the smectic–isotropic phase transition in ILCs depends on both the pore size and geometry as well as on the chemical structure of the ILC. Besides that, it was shown that the surface treatment of the pore walls directly influences the conductivity of confined smectic ILCs[19].

However, similar investigations for columnar ILCs in nano-confinement are not known to our best knowledge. It is crucial to understand how the confinement at a nanoscale (confinement size, surface wettability, etc.) affects the overall macroscopic properties such as charge transport and molecular dynamics, as it directly influences the end-use application of these novel functional materials. Herein, the phase behavior, the molecular dynamics as well as the conductivity for a columnar ILC confined to self-ordered anodic aluminum oxide nanopores ($180 \geq d \geq 25$ nm) are studied. It is investigated how the pore wettability, and the confinement size influences the molecular dynamics as well as the phase behavior. The DSC results reveal a suppression of the transition for columnar to the isotropic state while it is observed in the X-ray and dielectric investigations. This result is discussed in the framework of either a zero-entropy producing transition or as continuous second order transition. It is further demonstrated that the columnar self-assembly of ILC is dynamic and it slows down in confinement. Moreover, the formation of an interfacial layer for the ILC confined in 80 and 25 nm hydrophilic pores is detected, which is absent for the hydrophobic case. The results provide new insights into the restricted self-assembly and conductivity of nano-confined ILCs and can have broad implications towards understanding the dynamics and charge transport of soft matter in general. Moreover, the obtained results will have implications for the nanoscale applications of ionic liquid crystals.

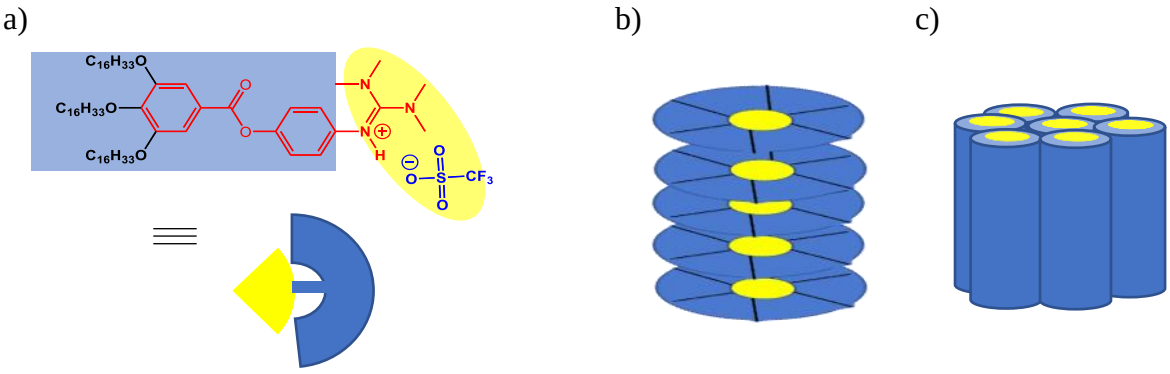

Figure 1. (a) Chemical structure of LC537. In red – aromatic core with the cation, blue – counter anion, black – alkyl side chains. Hydrophilic headgroup (yellow) containing ions, and hydrophobic body (blue) containing the aromatic core and alkyl chains. Six of this building molecules form a super disk. (b) Self-assembly of the superdiscs into an individual column. (c) self-assembly of individual columns in a 2D lattice.

Results and Discussion

Figure 1 gives the chemical structure of the investigated ILC called LC537. For details of the synthesis see ref.[21] With increasing temperature, the ILC can exhibits three distinct phases, the plastic crystalline (Cry), the hexagonal columnar (Col_h) and the isotropic phase (Iso). These phases are confirmed by X-ray scattering investigations and polarized optical microscopy.[21] In conventional discotic liquid crystals disc-like molecules form the columnar mesophase.[22] Nevertheless, for the ILC considered here still a columnar phase is observed, despite the building blocks are linear shaped molecules. Through ionic interactions, six linear shaped molecules form a disk-like structure which is referred as "*superdisc*" from this point onwards. For the hexagonal columnar phase, the superdiscs self-assemble into one-dimensional columns arranged in a 2D hexagonal lattice with the intercolumnar space filled with the flexible alkyl chains.

Self-ordered anodic aluminum oxide membranes with pores having diameters of 180, 80, 50, 40, and 25 nm were chosen as hosts for confinement (see Figure S1). The walls of the pores are hydrophilic in nature as produced. To study the influence of the nature of the pore walls a second set of membranes were prepared where the pore surfaces were modified with octadecylphosphonic acid (ODPA), so that the pore walls are coated by a nonpolar alkyl layer, making the pore walls hydrophobic. The thickness of this nonpolar layer was previously found to be around 2-3 nm[45]. ILCs confined in unmodified and modified pores are referred as the hydrophilic and hydrophobic scenarios, respectively.

Differential Scanning Calorimetry (DSC)

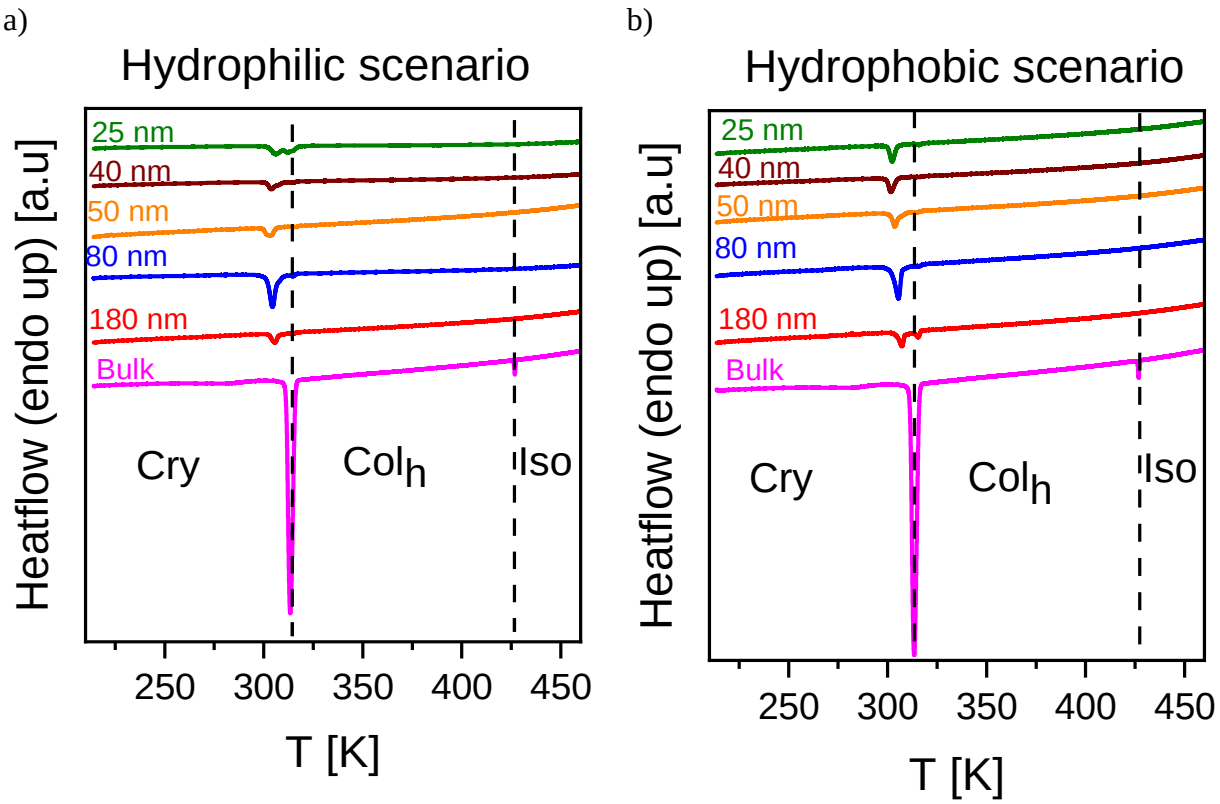

Figure 2. DSC heat flow curves for the bulk and the nanoconfined ILC. (a) in hydrophilic pores. The small peak observed in the hydrophilic case for a pore size of 25 nm is due to not removed bulk at the surface of the AAO membrane. (b) in hydrophobic pores. For sake of clarity the heat flow curves are shifted along the y-axis. The small peak observed in the hydrophobic case for a pore size of 180 nm is probably due to unremoved bulk material at the surface of the AAO membrane.[23] DSC thermograms for the heating run are provided in SI (Figure S2a).

Figure 2 displays the DSC thermograms for the ILC confined in (a) hydrophilic and (b) hydrophobic pores in comparison to the bulk. As discussed above for the bulk, three phases, the plastic crystalline phase (Cry) at low temperatures, the hexagonal columnar phase (Col_h) at higher temperatures, and the isotropic liquid phase (Iso) at the highest temperatures are observed. For both confined scenarios, the phase transition temperature of the Cry-Col_h transition decreases compared to the bulk with decreasing pore size. Surprisingly, the Col_h-Iso transition is not observed in the thermograms for both scenarios. Therefore, considered as suppressed in the thermal signal for all pore sizes. This result is further proofed in Figure SS2b and S3 in the Supporting Information where temperature range of the Col_h-Iso transition is enlarged. By a simple calculation given in the SI (paragraph enthalpy estimation), the expected enthalpy value of the columnar – isotropic transition for the confined sample is estimated from the enthalpies of the crystalline – columnar transition and columnar – isotropic transition of the bulk and is compared with the confined scenario. For the largest pore size of 180 nm this value

is calculated to be 0.1 J/g. This value is outside of the measuring errors of the device and therefore a small peak should be observed. In this connection it is worth to note that a suppression of the phase transition of polybutene-1 was reported recently.[24,25] At the first glance the disappearance of the Col_h-Iso transition in the DSC signal could be discussed by two possibilities: (i) LC537 remains in the Col_h phase in the considered temperature range or (ii) the Col-Iso phase transition takes place but is not observed by DSC as no entropy is related to it, or the entropic effects are compensated for this transition in confinement. Such an enthalpy entropy compensation (EEC) has been previously observed for polystyrene at confined interfaces[26].

The phase diagram for the Cry-Col_h transition is constructed as phase transition temperature versus inverse pore size (see Figure 3). Interestingly, the pore size dependence of the phase transition temperature $T_{Cry\text{-}Colh}$ cannot be described by the Gibbs-Thomson equation as found for other discotic liquid crystals and should be therefore expected[17,18]. Instead of a Gibbs-Thomson dependence, two regimes of the pore size dependence are observed. For large pore sizes the phase transition temperatures decrease as function of inverse pore size up to ca. 0.02 nm^{-1} (50 nm) followed by an increase of the transition temperatures for smaller pore sizes. The pore size dependence of the phase transition temperature can be empirically modelled by a combination of an exponential and linear relationship described by:

$$T_{Cry-Col_h} = p_1 * \exp\left[-\frac{1}{x*p_2}\right] + p_3 + p_4 * \frac{1}{x} \quad (1)$$

Here, x = 1/d, d is the pore diameter, for bulk d is taken as infinity, p_i, are the coefficients. The values of the coefficients are collected in table S1 in the SI.

It is interesting to state, that the hydrophilic scenario has a stronger pore size dependence compared to the hydrophobic counterpart. This concerns both the “exponential” as well as the “linear regime”. This behavior may have several molecular origins. Here it is assumed that for the hydrophobic scenario, there might be an interphase of the ODPA coating layer formed together with the building molecules of the ILC. Such an interphase was first discussed for confined rod-like and disc-like liquid crystals[17,18] and might directly influence the ordering of the ILC columns inside the pores. It is assumed that for the ILC in hydrophobic pores, the molecules will have different orientational order close to the pore wall rather than in the bulk.

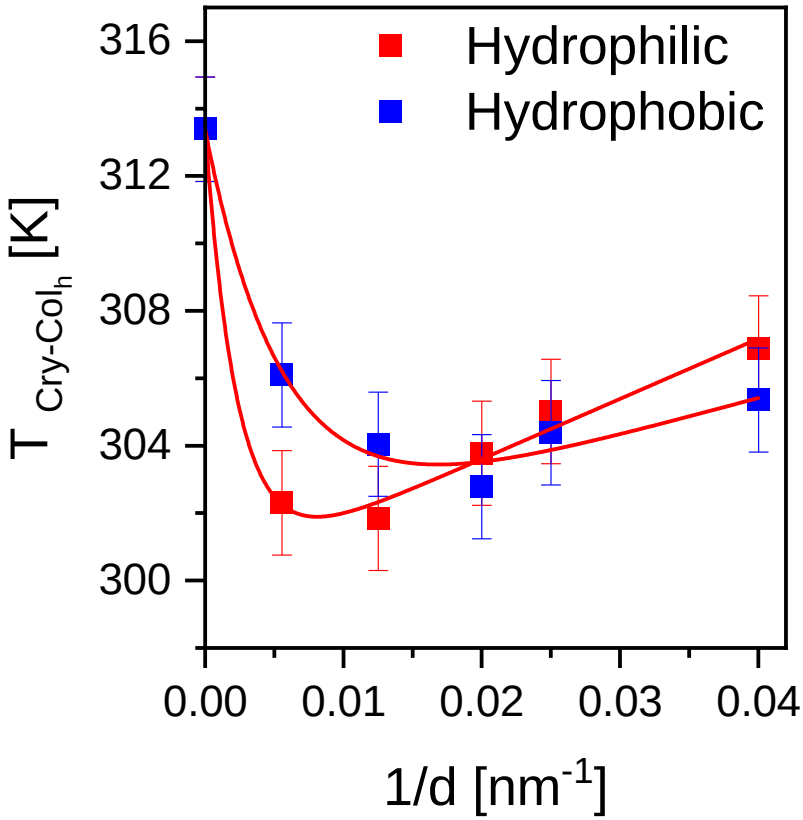

Figure 3. Phase transition temperature from the plastic crystal to the hexagonal ordered liquid crystalline state as a function of inverse pore size for the ILC confined to hydrophilic and hydrophobic pores as indicated. Solid lines are fits of a combination of an exponential and a linear relationship to the data (Eq. 1).

Broadband Dielectric Spectroscopy (BDS) – Molecular Dynamics

a)

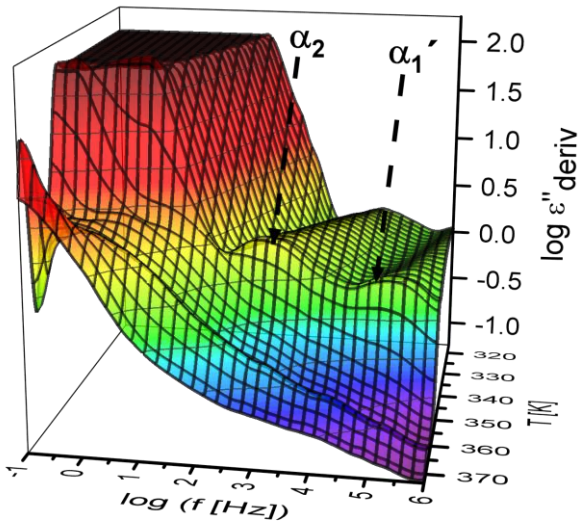

b)

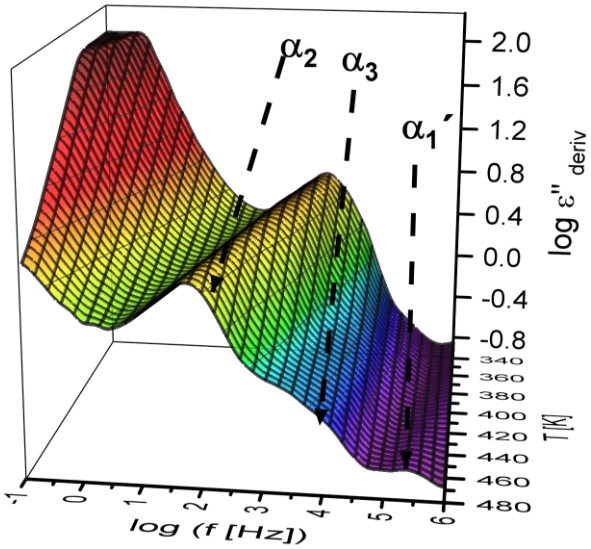

Figure 4. 3D plots of the conduction free dielectric loss (see text) in dependence of frequency and temperature: (a) Bulk and (b) ILC in hydrophilic pores with a diameter of 80 nm. Arrows indicate the relaxation modes.

Figure 4 depicts the 3D representation of the conduction free loss ε''_{deriv} (see method section)[47] for the bulk, and the ILC confined to hydrophilic pores with a diameter of 80 nm. As an example, the power of the conduction free loss analysis is demonstrated in Figure S4 where raw dielectric loss data are compared to that of the conduction free loss. For the bulk case, the dielectric spectra reveal two relaxation processes in the plastic crystalline phase, the γ relaxation and the α_1 relaxation. The two relaxation modes observed in the hexagonal columnar phase are denoted as α_1' and α_2 relaxation. Both latter relaxation processes could not be discussed in ref [29], because they were hidden by conductivity which is removed here by the conduction free loss analysis. At higher temperatures and low frequencies, the conduction free dielectric loss spectra show further increase of ε''_{deriv} with decreasing frequency. By the conduction free loss approach only ohmic contributions are removed from the dielectric spectra. The increase of ε''_{deriv} at higher temperatures and low frequencies indicates the presence of further contributions to the dielectric spectra like a Maxwell/Wagner/Sillars polarization which should be expected for a composite material. The γ relaxation takes place at low temperatures and is due to the localized fluctuations. This process will not be discussed further but some further data are given in the SI (Figures S5 – S7). For the bulk it would be interesting to compare the dielectric data for instance with mechanical ones. Unfortunately, due to the low sample amount obtained by the synthesis such measurements could not be carried out. For the confined scenarios, only the γ relaxation is observed in the plastic crystalline phase. The α_1 relaxation is suppressed (see also Figure S8, SI). The α_1' and the α_2 relaxation for the confined case is comparable to that of the bulk. The conduction free dielectric loss versus frequency of these relaxation modes is shown in Figure 5 for T = 343 K. The frequency of the peak maxima f_{max} of the relaxation processes (relaxation rates) were estimated by fitting the derivative of the real part of the Havriliak and Negami model function to the data.[47] The relaxation rates f_{max} are given versus inverse temperature in the Arrhenius plot (see Figure 7).

a) b)

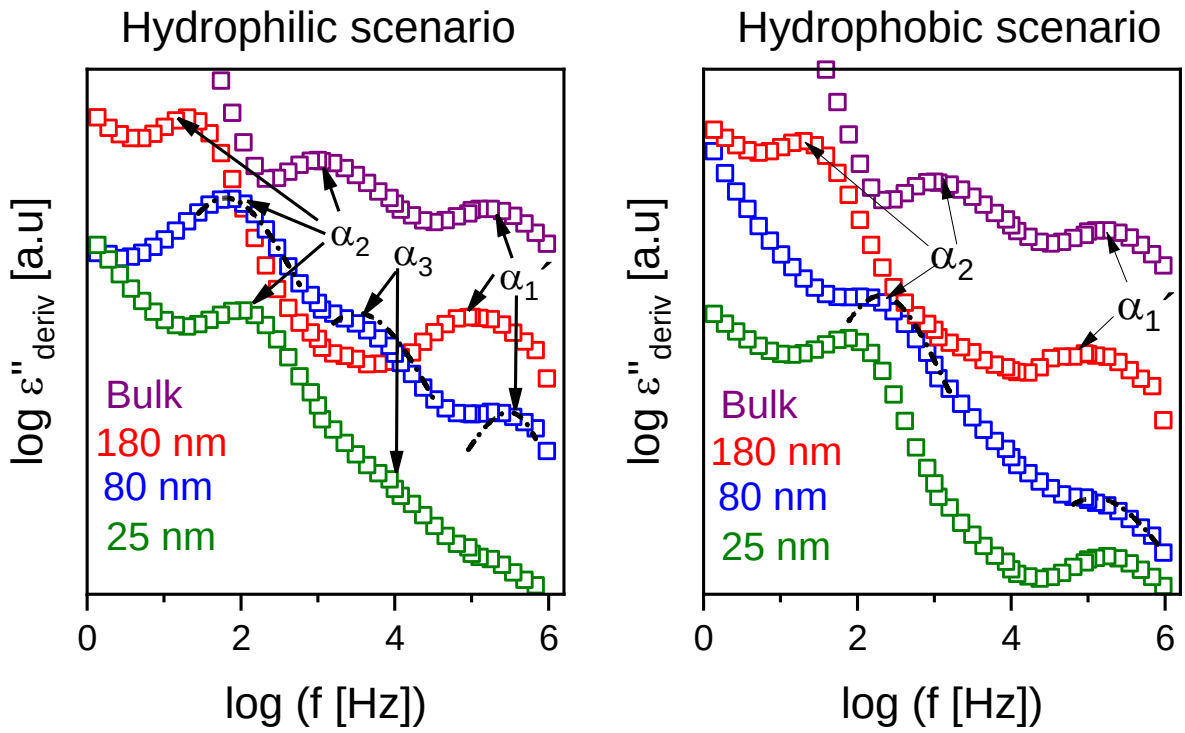

Figure 5. Isothermal representation of the conduction free loss at T = 343 K for the indicated pore sizes: (a) Hydrophilic scenario and (b) Hydrophobic scenario. Dash dotted lines are fits of the derivative of the real part of the Haviriliak and Negami function to the corresponding data. Examples for the fit parameters are given in the SI in Figure S9.

Restricted Spacer Mobility

The relaxation rates of the α_1 relaxation show a curved temperature dependence when plotted versus 1/T which indicates glassy dynamics as discussed earlier. [13,27] It can be described by the Vogel/Fulcher/Tammann (VFT) equation[28] as expected for glassy dynamics. (A fit of the Arrhenius equation leads to too high values of both the prefactor and the activation energy which cannot be explained physically.)

The VFT equation reads

$$log\ f_{max} = log\ f_{\infty} - \frac{A}{T-T_0} \qquad (2)$$

where f_∞ is a pre-exponential factor. Further A denotes a constant and the temperature T_0 is the Vogel or ideal glass transition temperature, which is located 30-70 K below the thermal glass transition temperature.

Previously, the α_1 relaxation of the bulk was related to cooperative fluctuations (glassy dynamics) of the alkyl side groups together with the cation headgroup.[13,29] This assignment is based by a combination of dielectric and AC chip calorimetry measurement. The relaxation rates of the α_1´ relaxation observed in the columnar phase, seems to have a similar the

temperature dependence of its relaxation rates as that of the α_1 relaxation. This is confirmed by the result that both data sets can be described by a common VFT fit. The α_1' relaxation is assigned to the mobility of the alkyl chains together with cation ion headgroup in the columnar phase. For both confined scenarios, the α_1 relaxation process is suppressed (see the previous section and Figure S8) which implies that confinement restricts the mobility of the alkyl side chains in the crystalline phase. In contrast, in the columnar phase the α_1' relaxation is observed for all pore sizes, except for the ILC confined in 25 nm hydrophilic pores. Probably the intensity of the α_1' relaxation process is too low to be observed for this pore size.

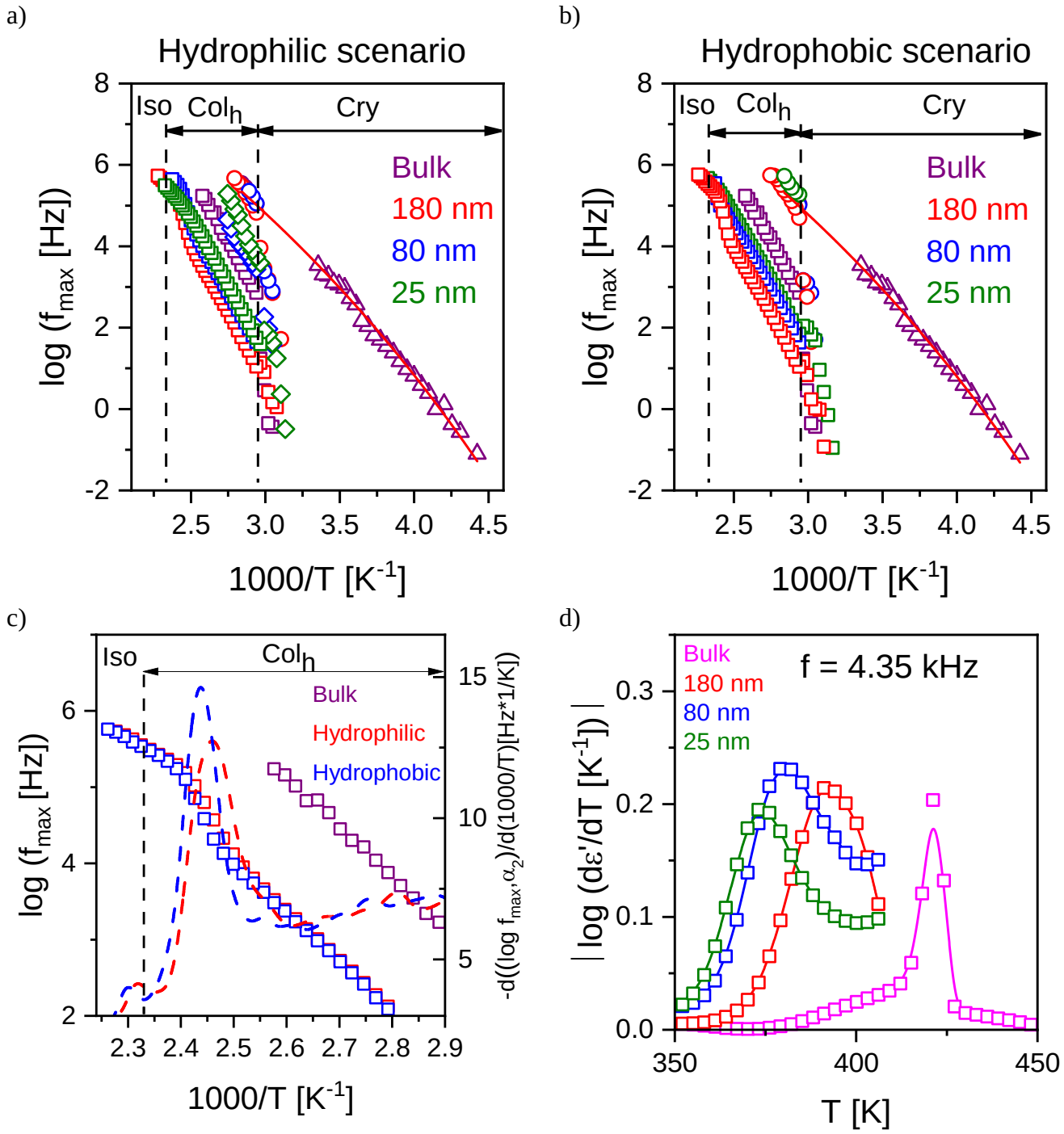

Figure 6. Arrhenius plot of the relaxation rates for the bulk and confined LC537. (a) the hydrophilic scenario and (b) the hydrophobic scenario. Up triangles – α_1 relaxation, squares – α_2 relaxation, circles – α_1' relaxation, diamonds – α_3 relaxation. The solid line is a common fit of the VFT equation to the relaxation rates of the α_1 and α_1' relaxation. (c) Comparison of the α_2 relaxation for bulk and LC537 in 180 nm pores. Dashed lines are the derivative of the relaxation rates versus inverse temperature. (d) Derivative of the real part of the complex permittivity versus temperature at a frequency of 4.35 kHz for the bulk and the ILC confined in hydrophilic pores. The lines are guides for the eyes.

Dynamic Structural Reorganization

The temperature dependence of the relaxation rates of the α_2 relaxation is compared for the bulk and the ILC confined in 180 nm pores (both hydrophilic and hydrophobic) in Figure 7c. The following is observed: (i) the α_2 relaxation for confined case is slower than for the bulk, (ii) the relaxation rates of the α_2 relaxation for the confined scenarios (both cases) exhibit a crossover behavior at around 410 K (see Figure 6c). The values of the relaxation rates below and above the crossover temperature (for confined scenarios), and that for the bulk, are linear when plotted versus 1/T and can be modeled by the Arrhenius function. The Arrhenius formular is given by

$$f_{max,\alpha_2} = f_\infty exp\left[-\frac{E_A}{RT}\right]. \quad (3)$$

Here, f_∞ is the relaxation rate at infinite temperatures, R is the universal gas constant and E_A symbolizes the apparent activation energy.

Before the molecular origin of the α_2 relaxation process is discussed, it should be kept in mind that the self-assembly of the building molecules of superdiscs forming one-dimensional columns is driven by non-covalent interactions such as coulombic interactions and hydrogen bonding[30,31]. These non-covalent interactions will enable an exchange of the building molecules of one superdiscs with building molecules of another one. This means that the self-assembly of the superdiscs is a dynamic process. This is especially true while considering that the superdiscs might have defects and that not always six building molecules form one superdisc. The apparent activation energy of the α_2 relaxation for the bulk, and for the confined scenarios (before the crossover) is around 120 – 130 kJ/mol. This value is too high for a dynamic hydrogen bond formation or dissociation but is in the range of ionic bond formation and dissociation due to coulombic interactions[32]. This suggests that the α_2 relaxation might be associated with the collective reorganization of superdiscs due to ionic (coulombic) interactions. This can be also discussed in the framework of network rearrangement, as it is reported for polymers with dynamic bonds (molecular stickers). Sokolov et al.[33] reported that for polymers with dynamic bonds, the network rearrangement occurs when one of the molecular stickers diffuse within the polymer matrix, creating an empty site, which is immediately occupied by a neighbored sticker. For ionic liquid crystals, a similar mechanism can be assumed. Here, instead of the diffusion of

a dynamic molecular sticker, the diffusion of individual building blocks of the superdiscs within a column is assumed. When one of the building blocks dissociates from a superdisc a vacancy site is created which is immediately occupied by a subsequent building block of a neighbored superdisc within the column. Thus, the α_2 relaxation reflects the dynamic rearrangement in the superdiscs within one column (see cartoon in Figure 7). Now, the crossover observed in the temperature dependence of the α_2 relaxation is discussed, as depicted in Figure 7c. The slope of the relaxation rate of the α_2 relaxation versus inverse temperature changes at the crossover, and the apparent activation energy decreases from 130 kJ/mol to around 70 kJ/mol. The derivative of the relaxation rates versus 1/T shows a maximum around the crossover. This maximum in the derivative and the reduction of the activation energy indicate that the material might be no longer in the columnar phase and enters the isotropic phase at the crossover temperature. In the isotropic phase the superdiscs no longer self-assemble in columns or the remaining columns have a higher disorder. This will ease the dynamic exchange of the building molecules between different superdiscs which leads to a lower activation energy of this process. Further it is known that the derivative of ε' regarding temperature is also sensitive towards phase transitions[17]. Figure 6d gives $d\varepsilon'/dT$ at a frequency of 4.35 kHz for the bulk and the ILC in hydrophilic pores. For the bulk, a narrow peak at around 424 K is observed, which is located around the temperature for the columnar to isotropic transition observed by DSC. For the confined scenario, also a peak is observed which is shifted to lower temperatures and broadened compared to the bulk. (The peak widths are compared in Figure S10 in the SI). The peak broadening observed for the confined scenario indicates that the phase transition is smeared across a broader temperature range compared to the bulk. This smearing out of the transition might be considered as continuous phase transition as first reported for confined nematic liquid crystal[34]. For the nematogen 7CB confined in nanoporous solids, a continuous nematic to isotropic transition was detected using BDS, where both the temperature dependence of relaxation modes and static capacitances show a continuous crossover[34]. Figure 9a gives the phase diagram of the columnar-isotropic transition for the bulk and confined ILC constructed by taking the temperature maxima of $d\varepsilon'/dT$. The Col_h – Iso transition temperature show a monotonic pore size dependence, which cannot be modelled by the Gibbs-Thomson equation. It is best described by an exponential relationship.

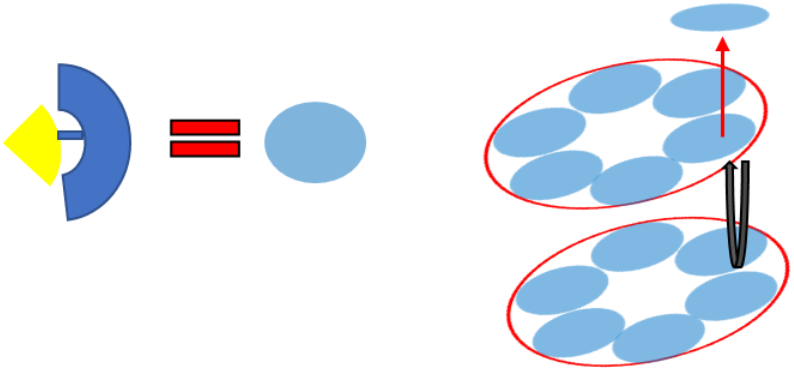

Figure 7. Cartoon for the molecular mechanism of the α_2 relaxation process. One individual ILC molecule (Yellow – hydrophilic part, blue – hydrophobic part) is represented as a light blue circle for simplicity. Red arrow indicates the creation of a vacancy cite by dissociation of one ILC molecule within an individual column. Black arrow indicates the subsequent rearrangement of a ILC layer within the column.

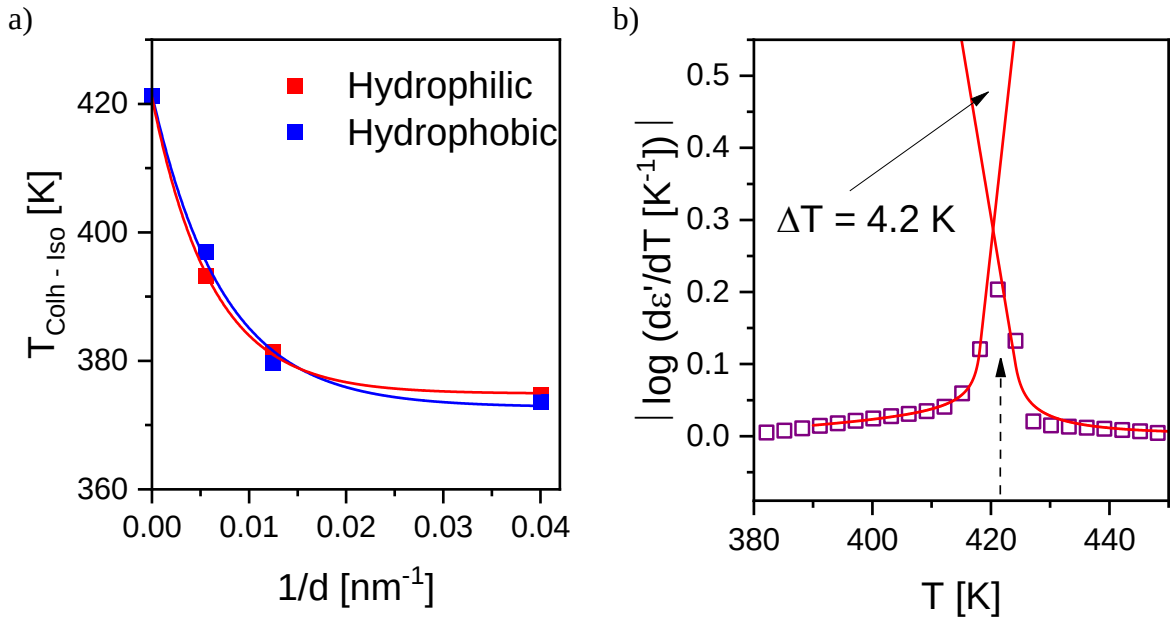

Figure 8. (a) Phase transition temperature from the hexagonal columnar to isotropic state as function of inverse pore size for the ILC confined to hydrophilic and hydrophobic pores as indicated. Solid lines are the exponential fit to the data. (b) Derivative of the real part of the dielectric permittivity as a function of temperature for the bulk ILC. Solid lines are fit of the eqns 4 and 5. Dashed arrow corresponds to the Col_h – Iso transition peak.

Structural Aspects

a) b)

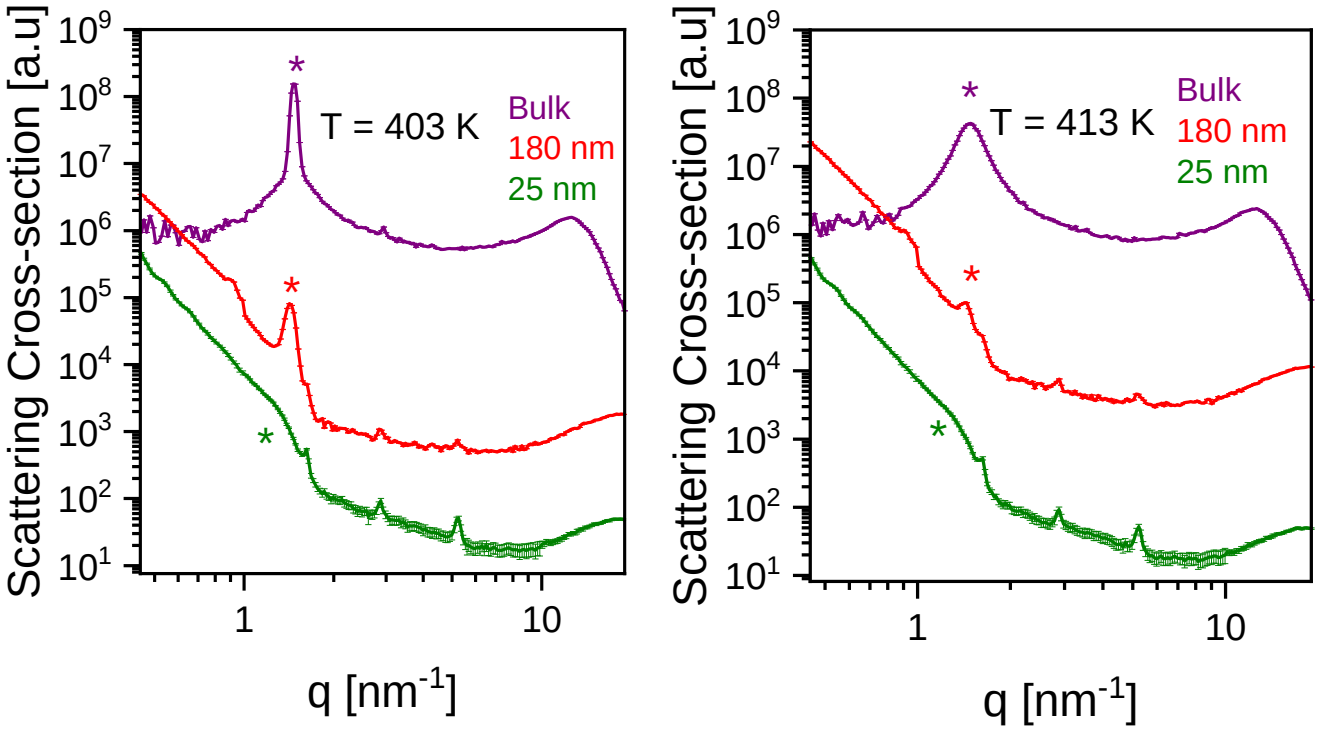

Figure 9. X-ray scattering pattern of LC537 in hydrophobic pores at the indicated temperatures and pore sizes. The sharp Bragg peaks for the confined sample between 2 and 8 nm^{-1} originate from the scattering of Aluminum which could not be removed completely. Stars (*) in (a) and (b) point to the (10) reflection of the bulk and confined ILC. The curves are shifted along the y-scales for sake of clarity.

To confirm the structural evidence of the columnar – isotropic transition observed by BDS, temperature dependent X-ray scattering studies were performed. Figure 10 shows the scattering pattern for the bulk, and the ILC confined in hydrophobic pores. At 403 K, the bulk and confined ILC show a relatively narrow peak, which is consistent with that expected for the (10) reflection of the hexagonal columnar phase. Besides the (10) reflection additional peaks should be expected at q position 1:31/2:41/2:71/2 for a columnar hexagonal ordered liquid crystalline phase.[35,36]. The absence of these peaks indicates probably a weakly ordered columnar phase. This conclusion is also supported by the small phase transition enthalpies a specially from the liquid crystalline to the isotropic phase. Nevertheless, the higher order reflections can be also weak for covalent bonded discotic molecules like triphenylene based discotic liquid crystals.[37] At the temperature T = 413 K where the ionic liquid crystal is expected to be in the isotropic phase, this peak becomes broader than that observed in the hexagonal columnar phase. The peaks observed in the isotropic phase indicate that there is some kind of remaining order of the superdiscs also in the isotropic phase. This means that the formation of the columns by the self-assembly of the superdiscs remains at least partly in the isotropic phase too. This conclusion is supported by Figure S11 where the distance between the columns a is plotted versus temperature. The distance a decreases continuously with temperature with no discontinuity at the phase transition. This dependence indicates that the Bragg peak in the liquid crystalline and

in the isotropic phase have a common origin. Nevertheless, it could not be excluded completely that the peak in the isotropic state does not reflect a columnar order. The temperature dependence of the distance between the columns is discussed in greater detail below. Assigning the peak in the isotropic phase to columns, the peak broadening indicates a higher disorder in the columns in the isotropic state compared to the hexagonal columnar phase[14,38]. The estimated transition temperature coincides with the crossover temperature observed for the α_2 relaxation (410 K). As discussed above the higher disorder in the columns may also ease the dynamic self-assembly of the superdiscs (α_2 relaxation). For the ILC confined to 25 nm, the (10) reflection of the columnar phase is subtle, but one can still see a kind of transition (indicated by a bump). For the confined sample with a pore size of 180 nm the (10) reflection can still be observed as a weak peak in the isotropic state. For the pore size of 25 nm still small bump might be detected. Besides the (10) reflection, a broad amorphous halo is observed for the bulk which corresponds to the average distance of the alkyl chains. For the confined case, the anodic aluminum oxide scatters more than the sample, and the halo at high q values includes contributions from both ILC and the anodic aluminum oxide. Hence an unambiguous deconvolution about the average distance of alkyl chain for the confined case cannot be made. The scattering curves for all measured temperatures are given in Figure S12. As discussed above from the (10) reflection, the columnar spacing *a* can be calculated for the bulk and confined ILC (see SI, eqn. S4). The temperature dependence of the columnar spacing *(a)* values are given in Figure S11 in the SI. In confinement for all temperatures the spacing between the columns is larger compared to the bulk. This result might indicate a higher disorder in the columns when confined to the nanopores. For the bulk the distance between the columns decreases linearly with increasing temperatures (compression of the columns). This result can be understood considering that the conformation of the alkyl side chains changes from a stretched conformation to a more coiled one. For both confinement scenarios the change of the distance between the columns is smaller and exhibit a kind of plateau at high temperatures. This result might indicate that the conformational changes of the alkyl side chain are restricted in confinement.

In Figure S3 (see SI) the phase transition temperature and the width of the columnar to isotropic transition obtained by the dielectric measurements is given in plot of the derivative of the heat flow versus temperature for ILC confined to pores with a diameter of 180 nm (both confinement scenarios). No change of the derivative of the heat flow is observed. This behavior indicates further that this phase transition is suppressed in the thermal signal for the confined ILC. Therefore, the columnar – isotropic transition, which is observed by the dielectric and scattering investigations can be considered as a zero-entropy producing transition as discussed for instance

for polymer crystallization[39] or as a continuous second order transition. To verify the critical behavior of the phase transition, and to describe degree of phase transition, equations based on a tricritical model[40] are used to model the temperature dependence of the real part of the dielectric permittivity data. The equations are given by

$$\left|\frac{d\varepsilon'}{dT}\right|_L = A + B_L\left|\frac{T-T^{**}}{T^{**}}\right|^{-\alpha} + C\left[\frac{T-T^{**}}{T^{**}}\right] \quad (4)$$

$$\left|\frac{d\varepsilon'}{dT}\right|_H = A + B_H\left|\frac{T-T^{*}}{T^{*}}\right|^{-\alpha} + C\left[\frac{T-T^{*}}{T^{*}}\right] \quad (5)$$

According to eqn 4 and 5, T^{**} and T^{*} denote the temperature at which the N-I transition would occur approaching from the nematic and isotropic state, respectively. The difference between T^{**} and T^{*}, i.e $\Delta T = T^{**} - T^{*}$, represent the width of the metastable region at the N-I phase transition. The existence of a metastable region is an indicative of a first order transition, and its absence refers to the second order transition. Here, α represents a critical exponent with a value of 0.5 for N-I transition. The subscripts L and H indicate the dielectric permittivity in the nematic and isotropic state, respectively. The parameters (A, B, C) are obtained through fitting the eqn 4 and 5 to the data. The analysis was carried out according to ref. 44 by excluding the coexistence region. An analysis including the coexistence was discussed by Floudas et al. elsewhere.[41,42] Although the experiments were carried out with a relatively low heating rate of ca. 0.4 K/min only few data points could be used because the transition is relatively sharp.

Selevou et al.[42], and Cusmin et al.[43], used the tricritical model to show that the nematic to istropic transition is first order in nature. Here, it is attempted to use tricritical model, though developed for Nematic – Isotropic transition, to check for the critical behavior of bulk and confined ILC at the Col_h – Iso transition. Fits were performed at either side of the $\left|\frac{d\varepsilon'}{dT}\right|$ peak corresponding to the Col_h – Iso transition using α=0.5. For the bulk, the fit yields divergence on either side of the Col_h – Iso transition peak and the virtual transition temperatures T^{**} and T^{*} are obtained through extrapolation. A metastable region of 4.2 K was calculated by $\Delta T = T^{**} - T^{*}$ (see Figure 9b). This value of the metastability region is in the range observed for other liquid crystalline systems exhibiting smectic, and nematic phase[42,44].

However, for the confined scenarios (both hydrophilic and hydrophobic), the model results in inadequate fits and cannot describe the $\left|\frac{d\varepsilon'}{dT}\right|$ at either side of the Col_h – Iso transition peak with

reasonable parameters, both with α=0.5 and for other values of it. More precisely, the values of the virtual transition temperatures (T^{**} and $T^{*)}$ are far from the temperatures of the actual Col_h – Iso transition peak and results in negative values for ΔT which cannot be explained on a physical basis. This is because, for the confined scenario, the Col_h – Iso transition peak is smeared across a broad temperature range, and not distinct as that for the bulk. The fit parameters for the bulk are given in SI (table S2).

Based on the above arguments, it is more likely that the Col_h – Iso transition for the confined scenarios, is a continuous second order phase transition, as opposed to discontinuous first order transition for its bulk counterpart. This is further supported from the thermal measurements where no change in the slope is observed in the derivative of the heat flow regarding to temperature at the Col_h – Iso transition (see Figure S2). Other possibilities such as zero-entropy transition or EEC might be ruled out for that reason.

Interfacial Layer dynamics

For the ILC in hydrophilic pores with pore diameters of 80 and 25 nm (see Figure 5a), a further relaxation mode, denoted as α_3 relaxation, is observed which is not there for the bulk and seems to be absent for the hydrophobic case (see Figure 5b). For the confined case this is further proved by Figure S13 comparing the dielectric spectra for the pore site of 80 nm for the hydrophilic and hydrophobic scenario. The relaxation rates f_{max} of α_3 process display a linear relationship when plotted versus inverse temperature. Therefore, this dependence can be described by the Arrhenius equation. The apparent activation energy of the α_3 process is found to be 113 kJ/mol and 154 kJ/mol for the ILC confined to pores of 80 and 25 nm in diameter, respectively. Since this process is observed only for the hydrophilic case with increasing confinement, this might reflect the collective dynamics of the building blocks, or the columns anchored near the pore wall surface. An ordering of columns near the pore walls has been previously reported for HAT6, and other liquid crystal molecules embedded in cylindrical nanopores[45],[18]. As interfacial process the α_3 relaxation is slower than the α_1 or the α_1' relaxation which are the corresponding processes where the molecules are not adsorbed. This is expected for an interfacial process. Interestingly, the apparent activation energy increases with increasing confinement (decreasing pore size). This can be due to an increasing Laplace pressure with decreasing pore size, as first discussed for a rod-like liquid crystal confined in anodic aluminum oxide nanochannels[17]. The ILC molecules confined in smaller pores experience more frustrations compared to that embedded in larger pores. Consequently, for smaller pores more

energy is required for the structural reorganization of the ILC molecule at the pore wall. Thus, a higher activation energy is observed for the ILC confined in pores with a diameter of 25 nm compared to the 80 nm. For the hydrophobic scenario, the pore walls are covered with long alkyl chain molecules. Probably the alky chains of the coating can interfere with the alkyl chains of the building blocks so that no strongly adsorbed interphase is formed[15,17]

Charge transport

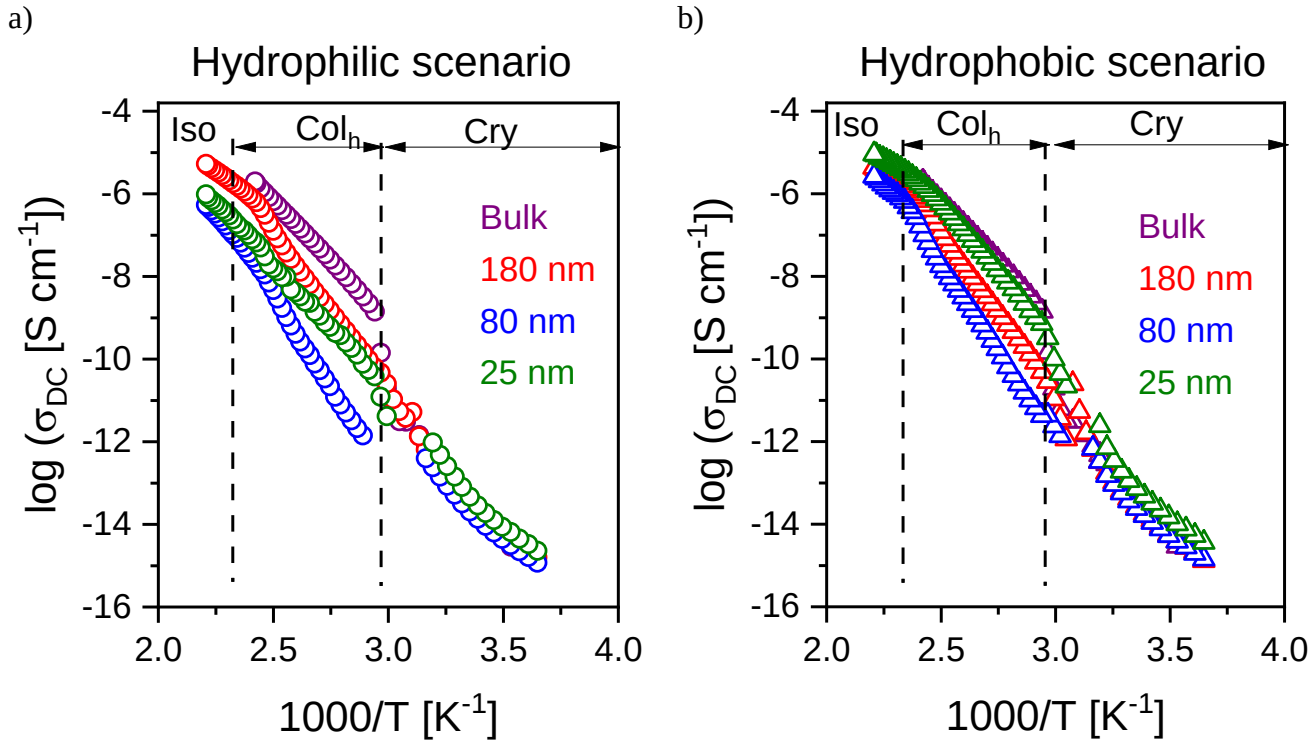

Figure 10. Arrhenius plot of the DC conductivity σ_{DC} for bulk and confined LC537. (a) Hydrophilic case and (b) Hydrophobic case.

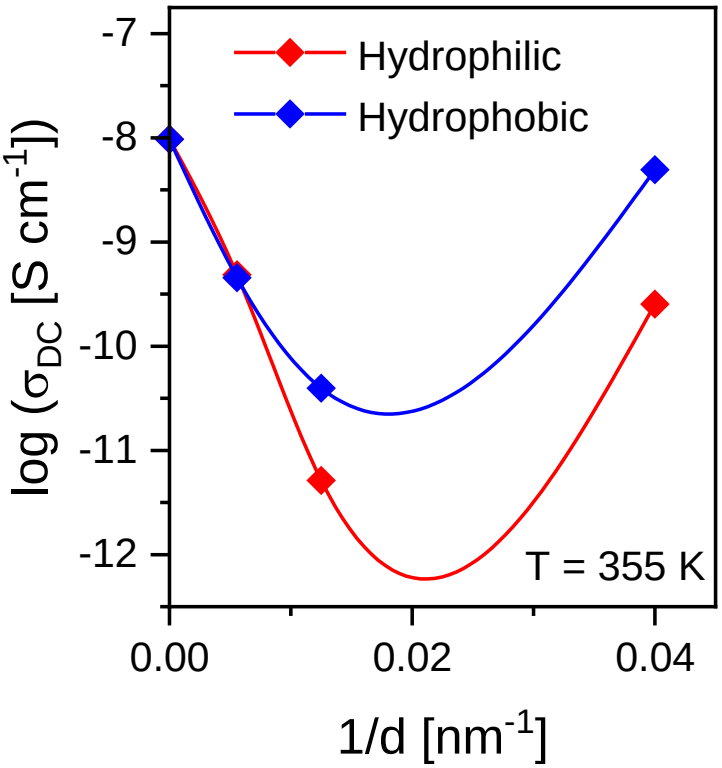

Figure 11. DC conductivity as function of inverse pore size at T = 355 K in the columnar phase. Solid lines are guides to eyes.

Besides the relaxation modes, a considerable DC conductivity is observed for all samples. The isothermal representation of the real part of the complex conductivity versus frequency is shown in the SI (see Figure S14) together with the estimation of the DC conductivity σ_{DC}. Before discussing the dependence of σ_{DC} on the temperature and pore size one has to note that the absolute values of the conductivity might be subjected to larger errors. On the one hand this might be due that the ILC in the pores is not in direct contact with the electrodes related to the meniscus formed during the filling of the pores as discussed by Tu et al. elsewhere.[46] This problem might be corrected by the suggested analysis of Tu et al. Such a correction was not carried here because the thermal behavior of the empty membranes was not stable. Nevertheless, it was shown that the influence of this corrections was relatively small.[46] On the other hand, the conductivity contribution was overlayed by strong electrode polarization effects. The correction for electrode polarization is difficult and might bear larger errors in σ_{DC}. But these errors are essentially smaller than the changes discussed below. Figure 10 depicts the DC conductivity in the Arrhenius plot for the confined scenarios compared to the bulk.

From Figure 11 the following is deduced: (i) For both the bulk and the confined scenarios, the absolute values of DC conductivity in the plastic crystalline phase have a linear dependence versus inverse temperature (ii) For the bulk, at the crystalline – columnar transition, a jump of 4 orders of magnitude is observed for the absolute values of the DC conductivity, for the

confined scenarios this jump is less pronounced and instead a continuous increase is observed with increasing temperature. It is worth to note that pretransition phenomena take place at the phase transition from the plastic crystalline to the liquid crystalline phase which are commonly observed for liquid crystalline systems. (iii) For the confined ILC, in the columnar phase, the temperature dependence of the absolute values of DC conductivity shows a cross over behavior similar to the temperature dependence of the relaxation rates of the α_2 relaxation. (iv) For the confined cases the conductivity increases at the transition from the liquid crystalline columnar phase to the isotropic state. The increase of the conductivity in the isotropic state is due to the fact that in the liquid crystalline state the mobility of the charge carriers is restricted due to the charge transport along the columns. At the phase transition the restricting liquid crystalline order disappears, and the ions are more free to move leading to a higher conductivity in the isotropic state.

For (i) and (ii), the following can be discussed: the DC conductivity has lower value in the crystalline phase because of the high viscosity in the crystalline phase, which restricts the drift mobility of the counter ion. In the columnar phase, ion channels are formed, and the counter ion can drift in these channels along the self-assembled columns, leading to a higher conductivity. For (iii), the crossover behavior reflects the columnar – isotropic transition in the conductivity data. By comparing the hydrophilic and hydrophobic scenarios, the ILC confined in hydrophobic pores with a diameter of 25 nm has σ_{DC} values approximately similar to the bulk. As an explanation for this behavior, it is assumed the lower values of the DC conductivity for the hydrophilic case might be due to the interfacial layer present near the pore walls, which can hinder the drift mobility of the counter ions. Figure 11 compares the dependence of the DC conductivity values versus pore size for both confined scenario. The DC conductivity as function of inverse pore size has qualitatively similar dependence on the pore diameter as that of the phase transition temperature of the Cry – Col_h transition (see Fig 4). The conductivity values decrease with decreasing pore size followed by an increase for the smallest pore size. This implies, that a critical pore size exists, with a different orientation of the ILC above and below this value. However, a direct relation between charge transport and phase transition temperature is difficult to establish and requires further investigation.

Conclusion

In this study a columnar ILC confined in self-ordered nanoporous anodic aluminum oxide membranes is investigated. For the confined case, the DSC results reveal a decreasing phase transition temperature with decreasing pore dimension of the Cry-Col_h transition, and a complete suppression of the Col_h – Iso transition. This result was further investigated employing BDS and X-ray scattering. Both X-ray scattering and BDS reveals the Col_h - Iso transition. Therefore, the Col_h – iso transition in confinement is discussed as a continuous phase transition, rather than as a discontinuous first order one.

The dielectric spectra show an α_1 relaxation for the bulk which is related to fluctuations of the alkyl side groups in the plastic crystalline phase. This relaxation process is not observed for the confined case. For both the bulk and confined scenarios, the α_2 relaxation process takes place in the columnar phase which was assigned to a dynamic self-assembly of the super discs within a column. The apparent activation energy values of the α_2 relaxation, which are in the range for values characteristic for ionic association and dissociation supports this assignment. Further, an interfacial relaxation process denoted as α_3 relaxation is observed for ILC confined in hydrophilic pores with diameters of 80 and 25 nm. This process is related to the structural organization of columns anchored near the pore walls. For the hydrophobic case this process is unobserved because the pore walls are covered with long nonpolar molecules which can interfere with the alkyl chains of the building blocks. The DC conductivity for the confined case, is in general reduced compared to the bulk. The conductivity values for the hydrophilic scenario are lower compared to the hydrophobic counterpart. It is assumed this might be due to the presence of interfacial layer for the hydrophilic case. Both the Cry – Col_h phase transition temperature and DC conductivity values have qualitatively similar pore size dependence. This result requires further investigations. The presented work provides a first insight about the behavior of confined columnar ionic liquid crystals in ordered nanochannels. The results are of technological relevance for the development of ILC based nano-devices with adjustable electrical, optical, and thermal properties.

Methods

Sample Preparation

Disk shaped anodic aluminum oxide (AAO) membranes with a thickness of 80 μm and diameter of 15 mm were obtained from Smart Membranes GmbH (Halle, Germany). The pore sizes ranging from 25 nm – 180 nm. The diameter of the pores and the porosity of the membranes given by the producer are listed in Table 1. Initially, the membranes were degassed at 473 K

under vacuum for 24 h to remove physical bounded impurities or adsorbed water as much as possible. The so-cleaned membranes were then moved under vacuum to a glove box which was filled with Argon. The amount of material needed to fill the pores completely was estimated based on the pore volume and porosity of the membranes assuming a density of 1 g/cm^3. The required amount of ILC along with a little excess was placed on the membranes and infiltrated at 444 K (20 K above the isotropic transition) for 48 h under argon conditions. Typical masses inside the membranes were in the range of few mg. Prior to all measurements, the excess amount of ILC was removed from the surface of AAO membranes as much as possible by a sharp knife. It was proofed by TGA measurements that the membranes were completely filled. TGA curves are given in Figure S14.

Table 1: Pore diameter and porosity of the employed AAO membranes.

Pore Diameter [nm]	Porosity [%]
25	10
40	10
50	14.5
80	37
180	14.5

The pore diameter and the porosity values are given by the producer. In ref. 45 these values are compared with own results. In general, relatively small differences are found which could not explain the found pore size dependence of the conductivity discussed above.

AAO Surface Modification

AAO membranes are inherently hydrophilic. To investigate the influence of the pore wettability, the pore walls surface was modified to change it to be hydrophobic. The surfaces of the pores were chemically modified with n-octadecylphosphonic acid (ODPA) employing a procedure reported in ref. [17]. ODPA was obtained from Alfa Aesar and used as delivered. The procedure is described briefly: (i) First, the pore walls of the membranes were activated with a 30% aqueous H_2O_2 solution at 45°C for 2h, and then dried at 120 °C for 15 min. The dried membranes were then soaked in to a 4mM solution of ODPA in a n-heptane/isopropyl alcohol mixture (volume ratio 5:1) at room temperature for 48 h. The membranes were later washed with substantial amounts of the n-heptane/isopropyl alcohol solution and sonicated for

15 min to remove any not adsorbed ODPA Then the membranes were dried under vacuum at room temperature overnight. The pore wall modification was confirmed by FTIR (see ref. 45).

Differential Scanning Calorimetry (DSC)

The thermal properties of the bulk and confined ILCs were investigated using a Perkin Elmer DSC 8500 setup. The specimen (ca. 6 mg) was placed in a standard pan of aluminum. The measurement was performed at temperatures from 203 K to 463 K employing rates of 10 K/min (heating and cooling). As purge gas Nitrogen is used. The flow rate was 20 ml/min. The scans are performed in the sequence heating / cooling / heating / cooling followed by a further heating step. The measured heat flow was subjected to a correction by subtracting the data of a measurement of an empty pan (baseline). This measurement was carried out at the same conditions than that of the sample. Prior to all measurements, a calibration procedure with Indium as a standard was performed.

Broadband Dielectric Spectroscopy (BDS)

The dielectric investigations were done by a high-resolution ALPHA analyzer (Novocontrol, Montabaur, Germany). This analyzer was interfaced to a sample holder which was equipped with an active sample head. The temperature of the sample was controlled by a Quatro temperature controller (Novocontrol). The temperature stability was better than 0.1 K. All the dielectric investigations were conducted in parallel plate geometry. For ILC in the bulk, the sample was placed between electrodes (gold plated brass) The diameter was 10 mm. A spacing of 50 μm between the two electrodes was obtained by placing fused silica spacers. For the ILC confined in AAO, the disklike membrane was placed between two gold plated electrodes with a diameter of 10mm. A spacing of 80 μm was provided by the thickness of the membrane. The confined ILC in AAO can be considered as two parallel plate capacitors composed of ILC in the pores and AAO, and the total permittivity is related to the individual values through,

$\varepsilon^*(f) = \varepsilon'(f) - i\varepsilon''(f)$ as complex dielectric function was measured by isothermal frequency scans in the window from 10^{-1} to 10^6 Hz. A temperature range of 133 K to 453 K was covered. ε' and ε'' are the real and imaginary part of the complex dielectric function. f denotes frequency. $i = \sqrt{-1}$ is the imaginary unit. The measurements were carried out as a sequence of heating / cooling and heating. It is noted that the dielectric loss is not scaled by the porosity. As only the relaxation rate is discussed quantitatively this procedure will cause no errors.

For relaxation processes in the columnar phase, the peak maxima were overlaid by a conductivity contribution. Hence the peaks were analyzed by the derivative technique, also called "conduction-free" dielectric loss (ε_{deriv}'') spectra[47]. For the Debye function

$$\varepsilon_{deriv}'' = -\frac{\partial \varepsilon'}{\partial log\omega} = (\varepsilon'')^2 \qquad (6)$$

is obtained. From Eqn (3), it is obvious that ε_{deriv}'' shows a peak like the dielectric loss. But this peak is narrower than that of ε′′. Any ohmic conductivity contribution is removed, since ε' is independent of frequency in that case. The ε_{deriv}'' are not corrected for the porosity because the permittivity of the AAO membranes are more or less independent of frequency. Therefore, the contribution of the membranes is removed by the derivative technique.

The relaxation processes were analyzed using the derivative Havriliak and Negami (HN) function. The HN function is given by[48],

$$\varepsilon^*_{HN} = \varepsilon_\infty + \frac{\Delta\varepsilon_{HN}}{(1+(i\omega\tau_{HN})^\beta)^\gamma} \qquad (7)$$

ε_∞ is the real part of ε^*in the limit of $\varepsilon_\infty = \lim_{\omega\to\infty} \varepsilon'(\omega)$. $\Delta\varepsilon_{HN}$ denotes the dielectric strength. τ_{HN} is the relaxation time which corresponds to the frequency of the maximum of the dielectric loss f_{max}. β and γ ($0 < \beta;\ \beta\gamma \leq 1$) describe the symmetric and asymmetric broadening of the relaxation spectrum compared to the Debye one[49].

For the HN-function, one obtains[47]

$$-\frac{\partial \epsilon'_{HN}}{\partial log\omega} = \frac{\beta\gamma\Delta\epsilon_{HN}(\omega\tau_{HN})^\beta \cos\left(\frac{\beta\pi}{2}\right)\left(-(1+\gamma)\Psi(\omega)\right)}{\left[1+2(\omega\tau_{HN})^\beta \cos\left(\frac{\beta\pi}{2}\right)+(\omega\tau_{HN})^{2\beta}\right]^{\frac{1+\gamma}{2}}} \quad (8)$$

Where $\Psi(\omega)$ is

$$\Psi(\omega) = \arctan\left[\frac{\sin\left(\frac{\beta\pi}{2}\right)}{(\omega\tau_{HN})^{-\beta}+\cos\left(\frac{\beta\pi}{2}\right)}\right] \quad (9)$$

For all relaxation processes the parameter γ is fixed to 1 during the analysis to reduce the number of free fit parameters.

The complex conductivity σ* is connected to ε* by

$$\sigma^*(\omega) = \sigma'(\omega) + i\sigma''(\omega) = i\omega\varepsilon_0\varepsilon^*(\omega). \quad (10)$$

$\sigma'(\omega)$ and $\sigma''(\omega)$ denote the real and imaginary components of the complex conductivity They are given by

$$\sigma'(\omega) = \omega\varepsilon_0\varepsilon''(\omega) \qquad (11)$$

and

$$\sigma'(\omega) = \omega\varepsilon_0\varepsilon'(\omega) \qquad (12)$$

The dependence of the real part of complex conductivity σ' on frequency was described by the empirical Jonscher power law[50]. The Jonscher equation is expressed as,

$$\sigma'(f) = \sigma_{DC}\left(1 + \left(\frac{f}{f_c}\right)^n\right) \qquad (13)$$

Here σ_{DC} is the DC conductivity. The exponent n has values between 0.5 and 1. The DC conductivity is connected to f_c versus the empirical Barton–Nakajima–Namikawa relation (BNN) relation[51]. The DC conductivity values were obtained by fitting the Johnscher equation to the data. For the confined case, the absolute values of DC conductivity are scaled with respect to the porosity of the membranes, such that

$$\sigma_{DC} = \frac{\sigma_{DC}}{\varphi} \qquad (14)$$

Here, φ is the porosity of the anodic aluminum oxide membrane.

X-ray Scattering

Temperature dependent small-/wide-angle X-ray scattering measurements were performed using the MOUSE device, a Xeuss 2.0 instrument (Xenocs, Grenoble, France) which is highly customized covering the SAXS and WAXS region.[52] X-rays were obtained from X-ray tube in a microfocus design. The target was copper. The obtained beam was treated by multilayer optics to parallelize and monochromatize it to the Cu K_α wavelength of 0.1542 nm. Data sampling was carried out using an Eiger 1M detector (Dectris, Baden, Switzerland) which was placed in vacuum at multiple position between 103 - 2507 mm from the sample. The samples were placed between two pieces of Kapton tape within a home-build in-situ heating cell and the temperature was increased, stepwise. X-ray data have been collected every 10 K from 303 K to 423 K. The obtained data has been carried out using the DAWN software package.[53,54] according to All procedures are standardized and considering background subtractions as well as a propagation of the errors.

Supporting Information

Dielectric dispersion for γ relaxation, X-ray Scattering curves at various temperatures (333 – 413 K), TGA curves.

Acknowledgement

The financial support by the German Research Foundation (DFG Project number 430146019 – AS/PH/SL) is acknowledged.

References

1. Laschat, S.; Baro, A.; Steinke, N.; Giesselmann, F.; Hägele, C.; Scalia, G.; Judele, R.; Kapatsina, E.; Sauer, S.; Schreivogel, A.; Tosoni, M. Discotic Liquid Crystals: From Tailor-Made Synthesis to Plastic Electronics. *Angewandte Chemie International Edition* **2007**, *46* (26), 4832–4887. https://doi.org/10.1002/anie.200604203.

2. Kapernaum, N.; Lange, A.; Ebert, M.; Grunwald, M. A.; Haege, C.; Marino, S.; Zens, A.; Taubert, A.; Giesselmann, F.; Laschat, S. Current Topics in Ionic Liquid Crystals. *ChemPlusChem* **2022**, *87* (1), e202100397. https://doi.org/10.1002/cplu.202100397.

3. Chen, S.; Eichhorn, S. H. Ionic Discotic Liquid Crystals. *Israel Journal of Chemistry* **2012**, *52* (10), 830–843. https://doi.org/10.1002/ijch.201200046.

4. Amano, S.; Ishida, Y.; Saigo, K. Solid-State Hosts by the Template Polymerization of Columnar Liquid Crystals: Locked Supramolecular Architectures around Chiral 2-Amino Alcohols. *Chemistry – A European Journal* **2007**, *13* (18), 5186–5196. https://doi.org/10.1002/chem.200601656.

5. Salikolimi, K.; Sudhakar, A. A.; Ishida, Y. Functional Ionic Liquid Crystals. *Langmuir* **2020**, *36* (40), 11702–11731. https://doi.org/10.1021/acs.langmuir.0c01935.

6. Marets, N.; Kuo, D.; Torrey, J. R.; Sakamoto, T.; Henmi, M.; Katayama, H.; Kato, T. Highly Efficient Virus Rejection with Self-Organized Membranes Based on a Crosslinked Bicontinuous Cubic Liquid Crystal. *Advanced Healthcare Materials* **2017**, *6* (14), 1700252. https://doi.org/10.1002/adhm.201700252.

7. Ishii, Y.; Matubayasi, N.; Watanabe, G.; Kato, T.; Washizu, H. Molecular Insights on Confined Water in the Nanochannels of Self-Assembled Ionic Liquid Crystal. *Sci Adv* **2021**, *7* (31), eabf0669. https://doi.org/10.1126/sciadv.abf0669.

8. Yoshio, M.; Mukai, T.; Ohno, H.; Kato, T. One-Dimensional Ion Transport in Self-Organized Columnar Ionic Liquids. *J. Am. Chem. Soc.* **2004**, *126* (4), 994–995. https://doi.org/10.1021/ja0382516.

9. Feng, X.; Tousley, M. E.; Cowan, M. G.; Wiesenauer, B. R.; Nejati, S.; Choo, Y.; Noble, R. D.; Elimelech, M.; Gin, D. L.; Osuji, C. O. Scalable Fabrication of Polymer Membranes with Vertically Aligned 1 Nm Pores by Magnetic Field Directed Self-Assembly. *ACS Nano* **2014**, *8* (12), 11977–11986. https://doi.org/10.1021/nn505037b.

10. Onuma, T.; Hosono, E.; Takenouchi, M.; Sakuda, J.; Kajiyama, S.; Yoshio, M.; Kato, T. Noncovalent Approach to Liquid-Crystalline Ion Conductors: High-Rate Performances and Room-Temperature Operation for Li-Ion Batteries. *ACS Omega* **2018**, *3* (1), 159–166. https://doi.org/10.1021/acsomega.7b01503.

11. Högberg, D.; Soberats, B.; Yatagai, R.; Uchida, S.; Yoshio, M.; Kloo, L.; Segawa, H.; Kato, T. Liquid-Crystalline Dye-Sensitized Solar Cells: Design of Two-Dimensional Molecular Assemblies for Efficient Ion Transport and Thermal Stability. *Chem. Mater.* **2016**, *28* (18), 6493–6500. https://doi.org/10.1021/acs.chemmater.6b01590.

12. Neidhardt, M. M.; Schmitt, K.; Baro, A.; Schneider, C.; Bilitewski, U.; Laschat, S. Self-Assembly and Biological Activities of Ionic Liquid Crystals Derived from Aromatic Amino Acids. *Phys. Chem. Chem. Phys.* **2018**, *20* (31), 20371–20381. https://doi.org/10.1039/C8CP03404D.

13. Kolmangadi, M. A.; Yildirim, A.; Sentker, K.; Butschies, M.; Bühlmeyer, A.; Huber, P.; Laschat, S.; Schönhals, A. Molecular Dynamics and Electrical Conductivity of Guanidinium Based Ionic Liquid Crystals: Influence of Cation Headgroup Configuration. *Journal of Molecular Liquids* **2021**, *330*, 115666. https://doi.org/10.1016/j.molliq.2021.115666.

14. Kolmangadi, M. A.; Smales, G. J.; ZhuoQing, L.; Yildirim, A.; Wuckert, E.; Eutionnat, S.; Demel, F.; Huber, P.; Laschat, S.; Schönhals, A. Side Chain Length-Dependent Dynamics and Conductivity in Self-Assembled Ion Channels. *J. Phys. Chem. C* **2022**, *126* (27), 10995–11006. https://doi.org/10.1021/acs.jpcc.2c03023.

15. Tu, W.; Jurkiewicz, K.; Adrjanowicz, K. Confinement of Pyrrolidinium-Based Ionic Liquids [CnMPyrr]+[Tf2N]− with Long Cationic Alkyl Side Chains (n = 10 and 16) to Nanoscale Pores: Dielectric and Calorimetric Studies. *Journal of Molecular Liquids* **2021**, *324*, 115115. https://doi.org/10.1016/j.molliq.2020.115115.

16. Tu, W.; Chat, K.; Szklarz, G.; Laskowski, L.; Grzybowska, K.; Paluch, M.; Richert, R.; Adrjanowicz, K. Dynamics of Pyrrolidinium-Based Ionic Liquids under Confinement. II. The Effects of Pore Size, Inner Surface, and Cationic Alkyl Chain Length. *Journal of Physical Chemistry C* **2020**, *124* (9) 5395–5408. https://doi.org/10.1021/acs.jpcc.9b10461.

17. Grigoriadis, C.; Duran, H.; Steinhart, M.; Kappl, M.; Butt, H.-J.; Floudas, G. Suppression of Phase Transitions in a Confined Rodlike Liquid Crystal. *ACS Nano* **2011**, *5* (11), 9208–9215. https://doi.org/10.1021/nn203448c.

18. Krause, C.; Schönhals, A. Phase Transitions and Molecular Mobility of a Discotic Liquid Crystal under Nanoscale Confinement. *J. Phys. Chem. C* **2013**, *117* (38), 19712–19720. https://doi.org/10.1021/jp406010d.

19. Uchida, Y.; Matsumoto, T.; Akita, T.; Nishiyama, N. Ion Conductive Properties in Ionic Liquid Crystalline Phases Confined in a Porous Membrane. *J. Mater. Chem. C* **2015**, *3* (24), 6144–6147. https://doi.org/10.1039/C5TC00314H.

20. Kohler, F. T. U.; Morain, B.; Weiß, A.; Laurin, M.; Libuda, J.; Wagner, V.; Melcher, B. U.; Wang, X.; Meyer, K.; Wasserscheid, P. Surface-Functionalized Ionic Liquid Crystal–

Supported Ionic Liquid Phase Materials: Ionic Liquid Crystals in Mesopores. *ChemPhysChem* **2011**, *12* (18), 3539–3546. https://doi.org/10.1002/cphc.201100379.

21 Butschies, M. Haenle, J. C.; Tussetschläger, S.; Laschat, S. Liquid Crystalline Guanidinium Phenylalkoxybenzoates: Towrds Room Temperature Liquid Crystals via Bending of the Mesogenic Core and he Use of Triflate Counterions. *Liq. Cryst.* **2013**, 40, 52-71.

22 Wöhrle, T.; Wurzbach, I.; Kirres, J.; Kostidou, A.; Kapernaum, N.; Litterscheidt, J.; Haenle, J. C.; Staffeld, P.; Baro, A.; Giesselmann, F.; Laschat, S. *Chem. Rev.* **2016**, 116, 1139 - 1241.

23 Shi, G.; Liu, G.; Su, C.; Chen, H.; Chen, Y.; Su, Y. Müller, A. J.; Wang, D. Reexamining the Crystallization of Poly(ε-caprolactone) and Isotactic Polypropylene under Hard Confinement: Nucleation and Orientation. *Macromolecules* **2017**, 50, 9015-9023. https://doi.org/10.1021/acs.macromol.7b02284

24 Shi, G.;Wang, Z.; Wang, M.; Liu, G.; Cavallo, D.; Müller, A. J.; Wang, D. Crystallization, Orientation, and Solid-Solid Crystal Transition of Polybutene-1 Confined within Nanoporous Alumina. *Macromolecules* **2020**, 53, 6510-6518. https://doi.org/10.1021/acs.macromol.0c01384

25 Ming, J. L.; Shi, G.; Liu, G.; Wang, L.; Cavallo, D.; Wang, D. Cooling Condition Determines the Transition Degree at Saturation of Form II in Isotactic Polybutene-1 Confined with Nanopores. Macromolecules 2022, 55, 7161-7170. https://doi.org/10.1021/acs.macromol.2c01041

26. McKenzie, I.; Fujimoto, D.; Karner, V. L.; Li, R.; MacFarlane, W. A.; McFadden, R. M. L.; Morris, G. D.; Pearson, M. R.; Raegen, A. N.; Stachura, M.; Ticknor, J. O.; Forrest, J. A. A β-NMR Study of the Depth, Temperature, and Molecular-Weight Dependence of Secondary Dynamics in Polystyrene: Entropy–Enthalpy Compensation and Dynamic Gradients near the Free Surface. *J. Chem. Phys.* **2022**, *156* (8), 084903. https://doi.org/10.1063/5.0081185.

27. Yildirim, A.; Szymoniak, P.; Sentker, K.; Butschies, M.; Bühlmeyer, A.; Huber, P.; Laschat, S.; Schönhals, A. Dynamics and Ionic Conductivity of Ionic Liquid Crystals Forming a Hexagonal Columnar Mesophase. *Phys. Chem. Chem. Phys.* **2018**, *20* (8), 5626–5635. https://doi.org/10.1039/C7CP08186C.

28. Kremer, F.; Schönhals, A. The Scaling of the Dynamics of Glasses and Supercooled Liquids. In *Broadband Dielectric Spectroscopy*; Kremer, F., Schönhals, A., Eds.; Springer: Berlin, Heidelberg, 2003; pp 99–129. https://doi.org/10.1007/978-3-642-56120-7_4.

29. Yildirim, A.; Szymoniak, P.; Sentker, K.; Butschies, M.; Bühlmeyer, A.; Huber, P.; Laschat, S.; Schönhals, A. Dynamics and Ionic Conductivity of Ionic Liquid Crystals

Forming a Hexagonal Columnar Mesophase. *Phys. Chem. Chem. Phys.* **2018**, *20* (8), 5626–5635. https://doi.org/10.1039/C7CP08186C.

30. Neidhardt, M. M.; Wolfrum, M.; Beardsworth, S.; Wöhrle, T.; Frey, W.; Baro, A.; Stubenrauch, C.; Giesselmann, F.; Laschat, S. Tyrosine-Based Ionic Liquid Crystals: Switching from a Smectic A to a Columnar Mesophase by Exchange of the Spherical Counterion. *Chemistry – A European Journal* **2016**, *22* (46), 16494–16504. https://doi.org/10.1002/chem.201602937.

31. Butschies, M.; Sauer, S.; Kessler, E.; Siehl, H.-U.; Claasen, B.; Fischer, P.; Frey, W.; Laschat, S. Influence of N-Alkyl Substituents and Counterions on the Structural and Mesomorphic Properties of Guanidinium Salts: Experiment and Quantum Chemical Calculations. *ChemPhysChem* **2010**, *11* (17), 3752–3765. https://doi.org/10.1002/cphc.201000444.

32. Samanta, S.; Kim, S.; Saito, T.; Sokolov, A. P. Polymers with Dynamic Bonds: Adaptive Functional Materials for a Sustainable Future. *J. Phys. Chem. B* **2021**, *125* (33), 9389–9401. https://doi.org/10.1021/acs.jpcb.1c03511.

33. Ge, S.; Samanta, S.; Li, B.; Carden, G. P.; Cao, P.-F.; Sokolov, A. P. Unravelling the Mechanism of Viscoelasticity in Polymers with Phase-Separated Dynamic Bonds. *ACS Nano* **2022**, *16* (3), 4746–4755. https://doi.org/10.1021/acsnano.2c00046.

34. Całus, S.; V. Kityk, A.; Eich, M.; Huber, P. Inhomogeneous Relaxation Dynamics and Phase Behaviour of a Liquid Crystal Confined in a Nanoporous Solid. *Soft Matter* **2015**, *11* (16), 3176–3187. https://doi.org/10.1039/C5SM00108K.

35 Pipertzis, A.; Zardalidis, G.; Wunderlich, K.; Klapper, M.; Müllen, K.; Floudas, G. Ionic Conductivity in Poly(ethylene glycol)-Functionalized Hex-peri-hexabenzocoronene Amphiphiles. *Macromolecules* **2017**, 50, 1981-1990. https://doi.org/10.1021/acs.macromol.7b00224

36 Wunderlich, K; Grigoriadis, C.; Zardalidis, G. Klapper, M.; Graf, R.; Butt, H.-J.; Müllen, K.; Floudas, G. Poly(ethylene glycol)-Functionalized Hexaphenylbenzenes as Unique Amphiphiles: Supramolecular Organization and Ion Conductivity. *Macromolecules* **2014**, 47, 5691-5702. https://doi.org/10.1021/ma501303k

37 Krause, C.; Zorn, R.; Emmerling, F.; Falkenhagen, J.; Frick, B.; Huber, P.; Schönhals, Andreas Vibrational density of states of triphenylene based discotic liquid crystals. Dependence on the length of the alkyl chain. *Phys. Chem. Chem. Phys.* 2014, 16, 7324-7333. https://doi.org/ 10.1039/c3cp55303e

38. Rivnay, J.; Noriega, R.; Kline, R. J.; Salleo, A.; Toney, M. F. Quantitative Analysis of Lattice Disorder and Crystallite Size in Organic Semiconductor Thin Films. *Phys. Rev. B* **2011**, *84* (4), 045203. https://doi.org/10.1103/PhysRevB.84.045203.

39. Toda, A.; Androsch, R.; Schick, C. Insights into Polymer Crystallization and Melting from Fast Scanning Chip Calorimetry. *Polymer* **2016**, *91*, 239–263. https://doi.org/10.1016/j.polymer.2016.03.038.

40. Mukhopadhyay, K.; Mukherjee, P. K. Density Effects in the Landau–De Gennes Theory Near the Nematic-Isotropic Phase Transition. *Int. J. Mod. Phys. B* **1997**, *11* (29), 3479–3489. https://doi.org/10.1142/S0217979297001738.

41 Selevou, A.; Papamoskos, G.; Steinhart, M.; Floudas, G. 8OCB and (CB Liquuid Crystals Confined in Nanoporous Alumina: Effect of Confinement on the Structure and Dynamics. *J. Phys. Chem. B* 2017, 121, 30. https://doi.org/10.1021/acs.jpcb.7b05042

42. Selevou, A.; Papamokos, G.; Yildirim, T.; Duran, H.; Steinhart, M.; Floudas, G. Eutectic Liquid Crystal Mixture E7 in Nanoporous Alumina. Effects of Confinement on the Thermal and Concentration Fluctuations. *RSC Adv.* **2019**, *9* (65), 37846–37857. https://doi.org/10.1039/C9RA08806G.

43. Cusmin, P.; de la Fuente, M. R.; Salud, J.; Pérez-Jubindo, M. A.; Diez-Berart, S.; López, D. O. Critical Behavior and Scaling Relationships at the SmAd−N and N−I Transitions in Nonyloxycyanobiphenyl (9OCB). *J. Phys. Chem. B* **2007**, *111* (30), 8974–8984. https://doi.org/10.1021/jp070689v.

44. Sarkar, S. K.; Das, M. K. Critical Behavior of Dielectric Permittivity in the Vicinity of Nematic–Isotropic and Smectic–Nematic Phase Transitions in Smectogenic Binary Mixtures. *Fluid Phase Equilibria* **2014**, *365*, 41–49. https://doi.org/10.1016/j.fluid.2013.12.010.

45. Yildirim, A.; Sentker, K.; Smales, G. J.; Pauw, B. R.; Huber, P.; Schönhals, A. Collective Orientational Order and Phase Behavior of a Discotic Liquid Crystal under Nanoscale Confinement. *Nanoscale Adv.* **2019**, *1* (3), 1104–1116. https://doi.org/10.1039/C8NA00308D.

46 Tu, W.; Richert, R.; Adranowicz, K. Dynamics of Pyrrolidinium-Based Ionic Liquids under Confinement. I. Analysis of Dielectric Permittivity. J. Phys. Che, C 2020, 124, 5389-5394. https://dx.doi.org/10.1021/acs.jpcc.0c00156

47. Wübbenhorst, M.; van Turnhout, J. Analysis of Complex Dielectric Spectra. I. One-Dimensional Derivative Techniques and Three-Dimensional Modelling. *Journal of Non-Crystalline Solids* **2002**, *305* (1), 40–49. https://doi.org/10.1016/S0022-3093(02)01086-4.

48. Havriliak, S.; Negami, S. A Complex Plane Analysis of α-Dispersions in Some Polymer Systems. *Journal of Polymer Science Part C: Polymer Symposia* **1966**, *14* (1), 99–117. https://doi.org/10.1002/polc.5070140111

49. Schönhals, A.; Kremer, F. Analysis of Dielectric Spectra. In *Broadband Dielectric Spectroscopy*; Kremer, F., Schönhals, A., Eds.; Springer: Berlin, Heidelberg, 2003; pp 59–98. https://doi.org/10.1007/978-3-642-56120-7_3.

50. Jonscher, A. K. The 'Universal' Dielectric Response. *Nature* **1977**, *267* (5613), 673–679. https://doi.org/10.1038/267673a0.

51. Dyre, J. C.; Schrøder, T. B. Universality of AC Conduction in Disordered Solids. *Rev. Mod. Phys.* **2000**, *72* (3), 873–892. https://doi.org/10.1103/RevModPhys.72.873.

52. Smales, G. J.; Pauw, B. R. The MOUSE Project: A Meticulous Approach for Obtaining Traceable, Wide-Range X-Ray Scattering Information. *J. Inst.* **2021**, *16* (06), P06034. https://doi.org/10.1088/1748-0221/16/06/P06034.

53. Filik, J.; Ashton, A. W.; Chang, P. C. Y.; Chater, P. A.; Day, S. J.; Drakopoulos, M.; Gerring, M. W.; Hart, M. L.; Magdysyuk, O. V.; Michalik, S.; Smith, A.; Tang, C. C.; Terrill, N. J.; Wharmby, M. T.; Wilhelm, H. Processing Two-Dimensional X-Ray Diffraction and Small-Angle Scattering Data in DAWN 2. *J. Appl. Crystallogr.* **2017**, *50* (Pt 3), 959–966. https://doi.org/10.1107/S1600576717004708.

54. Pauw, B. R.; Smith, A. J.; Snow, T.; Terrill, N. J.; Thünemann, A. F. The Modular Small-Angle X-Ray Scattering Data Correction Sequence. *J. Appl. Crystallogr.* **2017**, *50* (Pt 6), 1800–1811. https://doi.org/10.1107/S1600576717015096.

For Table of Contents Only: